Available online at www.sciencedirect.com
SCIENCE DIRECT®
Journal of Sound and Vibration 274 (2004) 801–819
JOURNAL OF SOUND AND VIBRATION
www.elsevier.com/locate/jsvi

Influence of permanent magnets on vibration characteristics of a partially covered sandwich cantilever beam

Huiming Zheng, He Zeng*

Department of Mechanics, Huazhong University of Science and Technology, Wuhan, Hubei Province 430074, People's Republic of China

Received 9 December 2002; accepted 2 June 2003

Abstract

The shear strains of viscoelastic damping layers resulting from the attraction arrangement magnets on the constraining layers root are higher than those of the conventional passive constrained layer damping treatment (PCLD). Therefore, significant improvement of damping characteristics can be achieved by using the new class of magnetic constrained layer damping treatment (MCLD). This paper presents an analytical modelling to elucidate vibration attenuation mechanism of the MCLD. It is shown that the variation amplitude of viscoelastic damping layers shear angle at the root where permanent magnets are fitted is relatively high, producing relatively high dynamic magnetic force compared to the maximal force on the constraining layers. The dynamic magnetic force is strong enough to reduce the elastic potential energy of the constraining layers and the primary layer and enhances the dissipation energy of the damping layers. The rise in the ratio of the dissipation energy to the total system energy per cycle suppresses the resonance peak. Furthermore, influences of permanent magnets on resonance peaks for the first several modes under different physical and geometrical properties are evaluated. Such evaluations are used to determine the merits and limitations of the MCLD treatment and develop design guidelines.
© 2003 Elsevier Ltd. All rights reserved.

1. Introduction

Passive constrained layer damping treatments (PCLD) have been extensively utilized, for many years, to damp out the vibration of flexible structures ranging from simple beams to complex space structures. In practice, partial damping treatment is necessary because of material, thermal, package, location and cost constraint [1]. Since the damping dissipation energy causes temperature rise in operation, the damping performance decreases. Moreover, the visco-elastic

*Corresponding author. Tel.: +27-87544740.
E-mail address: hezeng41@sohu.com (H. Zeng).

0022-460X/$ - see front matter © 2003 Elsevier Ltd. All rights reserved.
doi:10.1016/S0022-460X(03)00571-6

materials (VEM) of optimal shear modulus G are not always available, thus better damping performance is not always realized. In order to improve vibration reduction effects, numerous papers have reported active constrained layer damping treatments (ACLD) [2,3]. Although the ACLD treatments have proved to be successful in damping out structural vibration, they require the use of amplifiers and control circuits. As simplicity, reliability, practicality and effectiveness are our ultimate goal in controlling vibration and noise; the new concept of the magnetic constrained layer damping treatment (MCLD) with attraction arrangement magnets is introduced to eliminate the need for these circuits as well as any external energy [4,5]. But the vibration attenuation mechanism of the MCLD treatment versus the PCLD treatment and the effects of different physical and geometrical parameters on vibration reduction are not still understood clearly. In this paper, the differential equations of motion of a partially covered sandwich cantilever beam are derived employing Hamilton's principle. The modelling is validated experimentally. By analyzing the influence of permanent magnets on VEM's shear strains and force acting on the constraining layer (CL), the vibration attenuation mechanism of the MCLD treatment versus the PCLD treatment is clearly understood. The effects of different physical and geometrical parameters on resonance peaks are evaluated. Such evaluations are used to determine the merits and limitations of the MCLD treatments and to develop design guidelines.

2. Vibration analysis

2.1. Magnetic partial constrained layer damping treatment

The partial MCLD treatment of sandwich cantilever beam is illustrated in Fig. 1. Fig. 1(a) shows the undeflected configuration of the beam with permanent magnets of attraction arrangement fixed on the root of CL and in the base respectively, while Fig. 1(b) shows the deflected configuration under the action of an external bending moment **M**. When the beam is in the undeflected configuration, the static magnetic attractive forces produce static shear strains γ_0

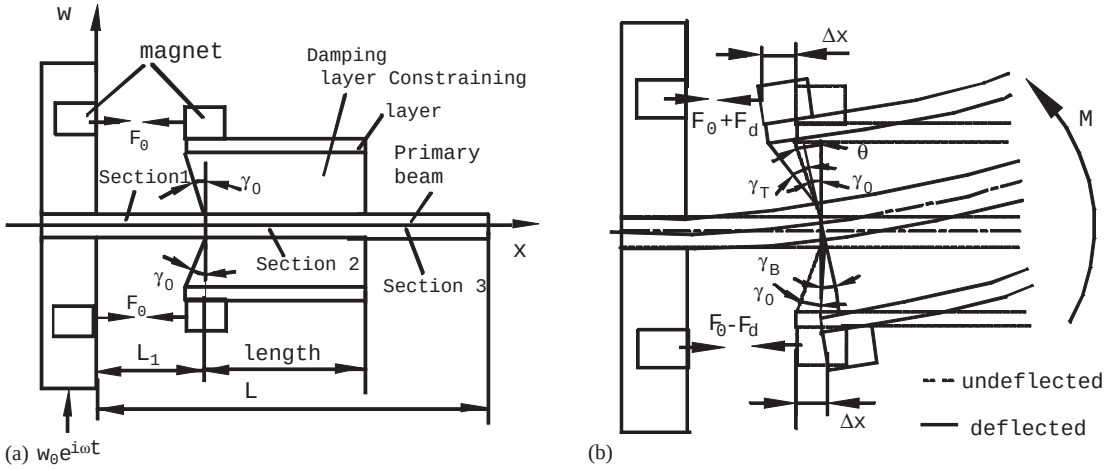

Fig. 1. Magnetic partially constrained damping treatment: (a) undeflected configuration, (b) deflected configuration.

in the top and bottom viscoelastic layers. In Fig. 1(b), due to the moment **M**, the gap between the top magnets decreases, causing magnetic attractive force to rise, the increment of shear strain $\gamma_{TM} = \gamma_T - \gamma_0$ is higher than the shear strain of the PCLD under external load of the same moment **M**. Further, the gap between bottom magnets rises, causing magnetic force to decrease, the variation value of shear strain is also larger than that of the PCLD. Increasing these shear strains enhances the energy dissipation. In this manner, significant improvement of the damping characteristics can be achieved.

2.2. Magnetic force

2.2.1. Magnetic induction density

The value of magnetic induction density d**B** at the point $S(0, R)$ shown in Fig. 2(a), which is produced by a straight wire of length a carrying a current **Q** along the x-axis can be calculated by

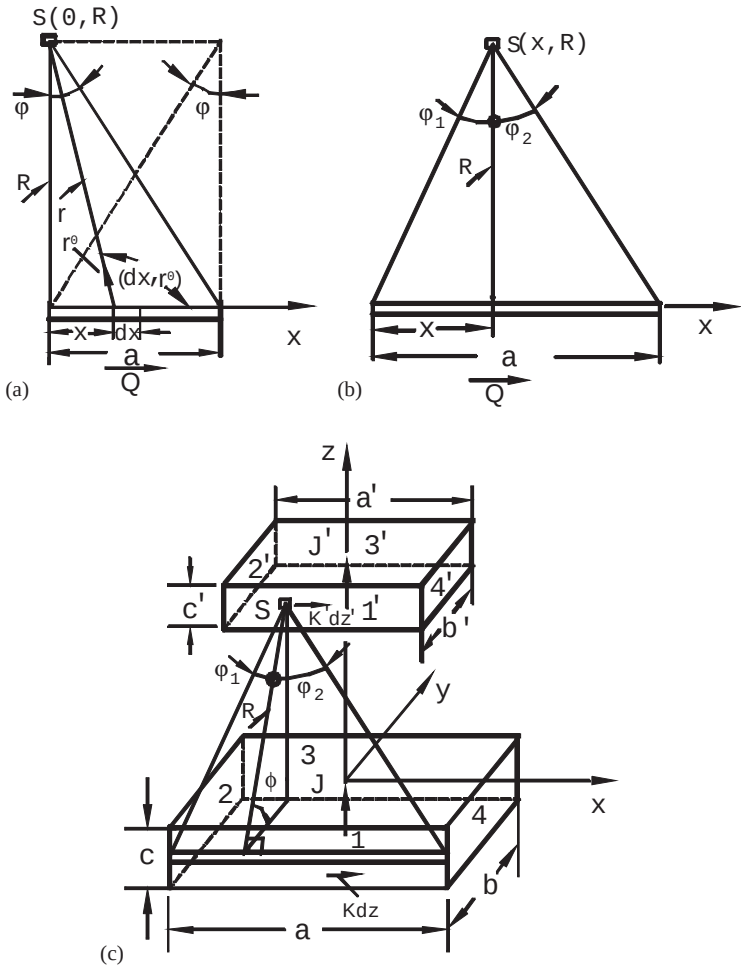

Fig. 2. (a) Magnetic induction d**B** at the point $S(0, R)$; (b) magnetic induction d**B** at the point $S(x, R)$, (c); permanent magnets configuration.

Biot–Savart's law:

$$d\mathbf{B} = \frac{\mu_0}{4\pi}\int_0^a \frac{|\mathbf{Q}\times\mathbf{r}^0|}{r^2}\,dx = \frac{\mu_0|\mathbf{Q}|}{4\pi}\int_0^a \frac{\sin(\mathbf{dx},\mathbf{r}^0)}{r^2}\,dx$$
$$= \frac{\mu_0|\mathbf{Q}|}{4\pi}\int_0^a \frac{R}{(R+x^2)^{3/2}}\,dx = \frac{\mu_0|\mathbf{Q}|}{4\pi R}\sin\varphi, \quad (1)$$

where $\mu_0 = 4\pi\times10^{-7}$ H/m, $\mathbf{r}^0$ is a vector, $d\mathbf{B}$ is directed out of the page in Fig. 2(a), $\sin\varphi = a/\sqrt{R^2+a^2}$.

In a like manner, the value of magnetic induction $d\mathbf{B}$ at the point $S(x,R)$ shown in Fig. 2(b) is also given by

$$d\mathbf{B} = \frac{\mu_0|\mathbf{Q}|}{4\pi R}(\sin\varphi_1 + \sin\varphi_2). \quad (2)$$

where $\sin\varphi_1 = x/\sqrt{R^2+x^2}$, $\sin\varphi_2 = (a-x)/\sqrt{R^2+(a-x)^2}$.

2.2.2. Magnetic force between two permanent magnets

The magnetic force between two permanent magnets in the shape of rectangular prisms of edge dimensions a,b,c and a',b',c', arranged as shown in Fig. 2(c), can be calculated by the Tsui's method in which the magnetic moment of a permanent magnet is represented by an equivalent face current loop [6–8]. It is assumed that each magnet is uniformly magnetized with magnetizations $\mathbf{J}$ and $\mathbf{J}'$ (Wb/m^2), oriented in the plus z direction. The magnets are represented by volume current densities $\mathbf{I}$ and $\mathbf{I}'$ (A/m^2) and by surface current densities $\mathbf{K}$ and $\mathbf{K}'$ (A/m). The volume current densities are given by

$$\mathbf{I} = \nabla\times(\mathbf{J}/\mu_0) \quad \text{and} \quad \mathbf{I}' = \nabla\times(\mathbf{J}'/\mu_0). \quad (3a,b)$$

The surface current densities are given by

$$\mathbf{K} = (\mathbf{J}/\mu_0)\times\mathbf{n} \quad \text{and} \quad \mathbf{K}' = (\mathbf{J}'/\mu_0)\times\mathbf{n}', \quad (4a,b)$$

where $\mathbf{n}$ and $\mathbf{n}'$ are unit vectors normal to the surfaces of the magnets. Since the magnets under discussion in this paper have a strong coercive force and it is magnetized uniformly inside, its volume currents vanish and only the surface currents exist.

For the magnet configuration in Fig. 2(c), $(a'\leqslant a, b'\leqslant b)$, the value of magnetic induction $d\mathbf{B}$ at an arbitrary point $S(x',y',z')$ on the side $1'$, which is produced by the current on the side 1, is given by

$$d\mathbf{B} = \int_{-c}^{0}\frac{\mu_0|\mathbf{K}|}{4\pi R}(\sin\varphi_1+\sin\varphi_2)\,dz, \quad (5)$$

where

$$R = \sqrt{(z'-z)^2+(-b'/2+b/2)^2}, \quad \sin\varphi_1 = (x'+a/2)/\sqrt{R^2+(x'+a/2)^2},$$
$$\sin\varphi_2 = (a/2-x')/\sqrt{R^2+(a/2-x')^2}.$$

For the adjacent sides 1 and 1′, only the component of the magnetic induction $d\mathbf{B}_y$ in the y direction produces attractive force in the z direction, thus

$$d\mathbf{B}_y = \int_{-c}^{0} \frac{\mu_0|\mathbf{K}|}{4\pi R}(\sin\varphi_1 + \sin\varphi_2 \sin\phi)\,dz, \tag{6}$$

where $\sin\phi = (z' - z)/R$.

The magnetic attractive force $d\mathbf{F}_z$ in the z direction at the point S produced by the surface currents on the side 1 is given by

$$d\mathbf{F}_Z = |\mathbf{K}'|dz'(d\mathbf{x}' \times d\mathbf{B}_y). \tag{7}$$

Thus the attractive force in the z direction between sides 1 and 1′ is given by

$$\begin{aligned} F_{1-1'} &= \int_{-a'/2}^{a'/2}\int_{d}^{d+c'} |\mathbf{K}'||\,d\mathbf{x}' \times\, d\mathbf{B}_y|\,dz' \\ &= \frac{\mu_0|\mathbf{K}'||\mathbf{K}|}{4\pi R}\int_{d}^{d+c'}\int_{-a'/2}^{a'/2}\int_{-c}^{0}(\sin\varphi_1 + \sin\varphi_2\sin\phi)\,dz\,dx'\,dz'. \end{aligned} \tag{8}$$

$F_{1-1'}$ can be obtained using numerical integration methods.

Repulsive forces between sides $1-3'$, $3-1'$, $2-4'$ and $4-2'$ and attractive forces between sides $2-2'$, $3-3'$ and $4-4'$ can also be calculated in a like manner. Since the magnetic induction $\mathbf{B}$ at an arbitrary point $S(x', y', z')$ on the side 2′ (or 4′), which is produced by the current on the side 1, is parallel to the side 2′ (or 4′), the magnetic force in the z direction between sides 1 and 2′ (or 4′) is zero.

By symmetry, the components of force in the y and x directions cancel one another; only the z direction components need to be calculated. The total attractive force F_m in the z direction is given by

$$F_m = 2(|\mathbf{F}_{1-1'}| + |\mathbf{F}_{2-2'}| - |\mathbf{F}_{1-3'}| - |\mathbf{F}_{2-4'}|). \tag{9}$$

Fig. 3 shows $\mathbf{J}$ versus the magnetic field $\mathbf{H}$ and $\mathbf{B}$ versus $\mathbf{H}$ hysteresis curves for ideal permanent magnets and the demagnetized curve of the magnet made of NdFeB. It can be seen that the magnetization $\mathbf{J}$ can be calculated from the relationship

$$\mathbf{B} = \mu_0\mathbf{H} + \mathbf{J}. \tag{10}$$

For a high-coercivity square-loop permanent magnet, $\mathbf{J}$ is equal to the residual induction $\mathbf{B}_r$ [6]. In fact, the value of the magnetization $\mathbf{J}$ varies slightly through the volume of such magnets and the condition of the magnet cannot be described by a single operating point, it is not possible to make a precise calculation of the actual force. It is reasonable, however, to calculate the approximate value on the basis of $|\mathbf{J}| = |\mathbf{B}_r|$ for the magnets made of NdFeB used in this study possessing the good square-loop demagnetization characteristics [6] shown in Fig. 3. When $\mathbf{K}$ is calculated on the basis of $|\mathbf{J}| = |\mathbf{B}_r|$, Eq. (9) gives the maximum magnetic force at the separation displacement. Note that, since the value $\mu_0|_B\mathbf{H}_c|$ is very close to $|\mathbf{B}_r|$ for magnets made of NdFeB blocks, it is also reasonable to calculate the magnetic force F_m on the basis of $|\mathbf{J}| = \mu_0|_B\mathbf{H}_c|$.

Fig. 4 illustrates the variation of attractive force F_m with the gap d between two magnets made of NdFeB blocks ($20 \times 5 \times 5$ mm) with residual induction $B_r = 11,900$ G and the demagnetized coercive force ${}_BH_c = 10,630$ Oe and the intrinsic coercive force ${}_JH_c = 17,660$ Oe. It can be seen

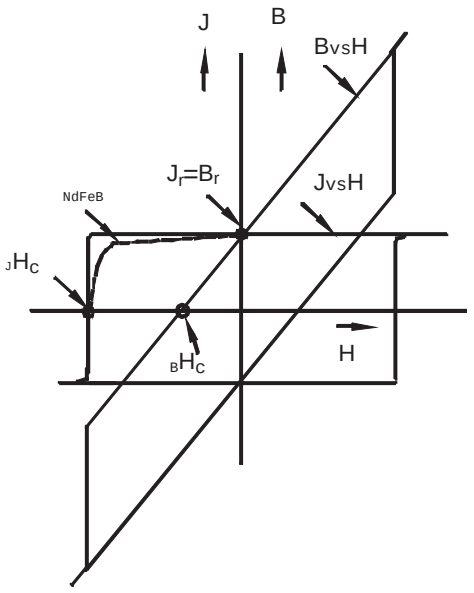

Fig. 3. **J** versus **H** and **B** versus **H** hysteresis curves for ideal magnets and demagnetized curve of the magnet made of NdFeB.

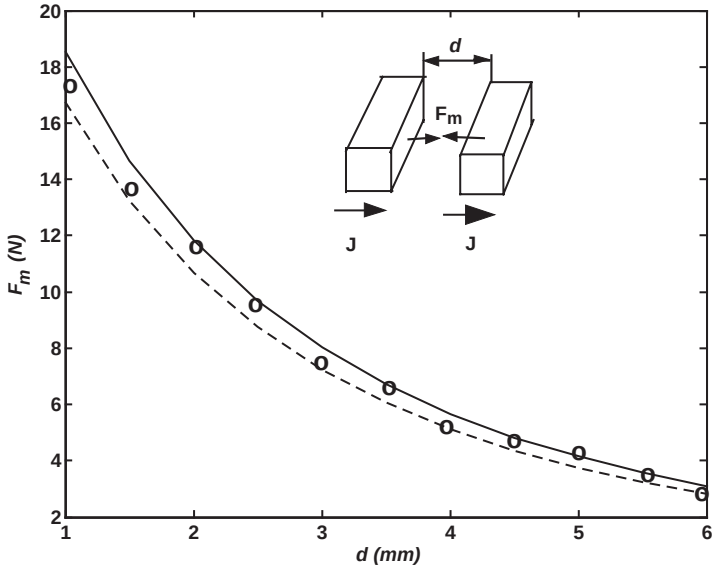

Fig. 4. Variation of attractive force F_m with the gap d between two magnets (calculation: —, $|\mathbf{J}| = |\mathbf{B}_r|$; - - -, $|\mathbf{J}| = \mu_0|_B\mathbf{H}_c|$; experiment: o).

that the magnetic forces F_m on the basis of $|\mathbf{J}| = |\mathbf{B}_r|$ or $|\mathbf{J}| = \mu_0|_B\mathbf{H}_c|$ are in good agreement with experimental results. The perfect agreement between experimental and analytical results (maximum force, $|\mathbf{J}| = |\mathbf{B}_r|$) was also observed for the magnets with good square-loop demagnetization characteristics in a previous paper [6].

2.3. Basic equations

The beam can be separated into three sections (see Fig. 1(a)). Section 2 is a double sandwich-type beam, and Sections 1 and 3 are ordinary beams. The differential equation of motion for Section 1 is governed by (see Fig. 5(b)),

$$D_{t1}\left(\frac{\partial^4 w_1}{\partial x^4}\right) + m_1\left(\frac{\partial^2 w_1}{\partial t^2}\right) = 0. \tag{11}$$

The boundary conditions are

$$x = 0: \quad w_1(x) = w_0 e^{i\omega t}, \quad \frac{\partial w_1(x)}{\partial x} = 0,$$
$$x = L_1: \; D_{t1}\frac{\partial^2 w_1}{\partial x^2} = M_2, \quad D_{t1}\frac{\partial^3 w_1}{\partial x^3} = S_2. \tag{12a–d}$$

Now let us consider the vibration of Section 2. The following assumptions are made in the analysis: (1) the beam deflection is small and uniform across any section; (2) the primary beam and the upper and lower constraining beams are assumed to be isotropic; (3) the longitudinal and rotary inertia effects of the beam are neglected; (4) the damping layers carrying shear, but no direct stress, are assumed to be linear viscoelastic; and (5) no slip occurs at the interface between the layers.

To simplify analysis, assuming the double sandwich beam to be symmetric, we choose static equilibrium state as a reference. The longitudinal displacements and shear angles in the following refer to the variation relative to the reference. Thus we have the relationships (see Fig. 5(a)):

$$u_3 = -u_4, \quad \frac{\partial u_3}{\partial x} = -\frac{\partial u_4}{\partial x}, \quad \frac{\partial u_1}{\partial x} = 0. \tag{13a–c}$$

The potential energy of Section 2 is

$$V = (V_1 + V_3 + V_4)_{bending} + (V_1 + V_3 + V_4)_{extension} + (V_{c1} + V_{c2})_{shearing},$$

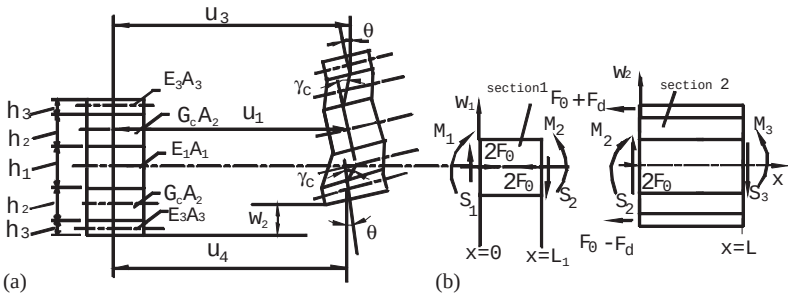

Fig. 5. The deformation and loads: (a) the geometry and deformation of Section 2; (b) Sections 1 and 2 with loads and moments.

$$(V_1 + V_3 + V_4)_{bending} = \frac{1}{2}\int_{L_1}^{L_2} D_t\left(\frac{\partial^2 w_2}{\partial x^2}\right)^2 \mathrm{d}x$$

$$(V_1 + V_3 + V_4)_{extension} = \int_{L_1}^{L_2} E_3 A_3\left(\frac{\partial u_3}{\partial x}\right)^2 \mathrm{d}x,$$

$$(V_{c1} + V_{c2})_{shearing} = \int_{L_1}^{L_2} G_c A_2 \gamma_c^2 \,\mathrm{d}x. \tag{14a–d}$$

In Fig. 5(a), we have the relationships

$$u_1 - u_4 = h_2\gamma_c - H\theta, \quad u_3 - u_1 = h_2\gamma_c - H\theta \tag{15a, b}$$

thus $u_3 = h_2\gamma_c - H\theta$, $\gamma_c = (u_3 + H\theta)/h_2$, where $H = h_2 + (h_1 + h_3)/2$.

After neglecting longitudinal and rotary inertia and assuming the mass of permanent magnets to concentrate at $x = L_1$, the total kinetic of the Section 2 is

$$T = \frac{1}{2}\int_{L_1}^{L_2}\left[m\left(\frac{\partial w_2}{\partial t}\right)^2 \mathrm{d}x\right] + m_{mag}\left(\frac{\partial w_2}{\partial t}\right)^2\Bigg|_{x=L_1}. \tag{16}$$

Since the length of Section 1 is very short, the effect of pressure on work is negligible. The work done by external force is given by

$$W = \left[-M_2\left(\frac{\partial w_2}{\partial x}\right) + S_2 w_2\right]\Bigg|_{x=L_1} + W_{mag}\big|_{x=L_1} + \left[M_3\left(\frac{\partial w_2}{\partial x}\right) - S_3 w_2\right]\Bigg|_{x=L_2}, \tag{17}$$

where W_{mag} is the work done by magnetic force F_m. F_m is the x direction component of the magnetic force. $F_m = F_0 \pm F_d, F_0$ is the static component, F_d is the dynamic component resulting from the gap variation Δx between magnets.

$$F_d = (\partial F_m/\partial x|_{x=L_1})\Delta x, \tag{18}$$

where $\Delta x = h_2\gamma_c + H_n(\partial w_1/\partial x|_{x=0} - \partial w_2/\partial x|_{x=L_1}), H_n = h_2 + h_3 + (h_1 + h_{mag})/2$.

Since the sum of the work done by F_0 acting on the primary and constraining layers is zero, work done by F_d is only considered. The effect of two pairs of magnets is equivalent to a spring of negative stiffness

$$K_d = -2(\partial F_m/\partial x)|_{x=L_1}. \tag{19}$$

Applying Hamilton's principle

$$\delta\int_{t_1}^{t_2}(T - V + W)\,\mathrm{d}t = 0 \tag{20}$$

we obtain the differential equations of motion of Section 2

$$D_t\frac{\partial^4 w_2}{\partial x^4} - NH\left(H\frac{\partial^2 w_2}{\partial x^2} + \frac{\partial u_3}{\partial x}\right) + m\frac{\partial^2 w_2}{\partial^2 t} = 0, \tag{21}$$

$$-2E_3A_3\frac{\partial^2 u_3}{\partial x^2} + N\left(H\frac{\partial w_2}{\partial x} + u_3\right) = 0. \tag{22}$$

In addition, Hamilton's principle yields the following beam boundary conditions:

$$x = L_2\colon\ D_t \frac{\partial^2 w_2}{\partial x^2} = M_3, \quad -D_t \frac{\partial^3 w_2}{\partial x^3} + NH\left(H\frac{\partial w_2}{\partial x} + u_3\right) = -S_3, \quad 2E_3A_3\frac{\partial u_3}{\partial x} = 0,$$

$$x = L_1\colon\ -D_t \frac{\partial^2 w_2}{\partial x^2} + M_2 - K_d(H - H_n)\left[(H - H_n)\frac{\partial w_2}{\partial x} + u_3\right] = 0, \tag{23a–c}$$

$$D_t \frac{\partial^3 w_2}{\partial x^3} - NH\left(H\frac{\partial w_2}{\partial x} + u_3\right) - S_2 + 2m_{mag}\frac{\partial^2 w_2}{\partial t^2} = 0,$$

$$-2E_3A_3\frac{\partial u_3}{\partial x} - K_d\left[(H - H_n)\frac{\partial w_2}{\partial x} + u_3\right] = 0, \tag{24a–c}$$

where $N = 2G_c b_0/h_2$.

2.4. Vibration analysis

To solve Eqs. (21) and (22) for harmonic vibrations, assume the solution to be of the form [9]

$$\begin{Bmatrix} w_2 \\ u_3 \end{Bmatrix} = \begin{Bmatrix} w_{2n} \\ u_{3n} \end{Bmatrix} e^{kx} e^{i\omega t}, \tag{25}$$

where k denotes the unknown complex characteristic value, and ω denotes the excitation frequency. Substituting the expression for w_2 and u_3 into Eqs. (21) and (22) and eliminating u_3, we have

$$k^6 + s_2k^4 + s_1k^2 + s_0 = 0, \tag{26}$$

where $s_2 = -(2E_3A_3NH^2 + ND_t)/(2E_3A_3D_t)$, $s_1 = -m\omega^2/D_t$, $s_0 = m\omega^2N/(2E_3A_3D_t)$.

From Eq. (26), it can be seen that for any value of ω, there would be six complex values of k. Let k_{2i} $(i = 1, 2, \ldots, 6)$ denote the six zeros of Eq. (26), we then have, for Section 2,

$$w_2(x) = \sum_{i=1}^{6} C_{2i}e^{k_{2i}x}, \tag{27}$$

where C_{2i}, k_{2i} denote a complex value.

From Eqs. (21) and (22), we have

$$u_3(x) = \sum_{i=1}^{6} g_{2i}C_{2i}e^{k_{2i}x}, \tag{28}$$

where $g_{2i} = 2E_3A_3D_tk_{2i}^5/(N^2H) - 2E_3A_3Hk_{2i}^3/N - [2E_3A_3m\omega^2/(N^2H) + H]k_{2i}$ $(i = 1, 2, \ldots, 6)$. For Section 1, assume the solution to be of the form

$$w_1(x) = \sum_{i=1}^{4} C_{1i}e^{k_{1i}x}, \tag{29}$$

where C_{1i} and k_{1i} denote complex values.

Repeating the above approaches, we can obtain the differential equation of motion and boundary conditions of Section 3. Also, the continuous conditions of transverse displacement w

and rotary angle θ at $x = L_i$ $(i = 1, 2)$, yield supplementary conditions. The boundary equations and supplementary conditions can be placed in a matrix representation to solve for the unknown complex coefficients C_{ji} by standard matrix inversion methods or $[\mathbf{D}]\{\mathbf{C}\} = \{\mathbf{W}\}$. The following expressions at arbitrary point in Section 2 can be deduced:

$$w_2(x,\omega,t) = W_0 \sum_{i=1}^{6} C_{2i} e^{k_{2i}x+i\omega t}, \quad \theta(x,\omega,t) = W_0 \sum_{i=1}^{6} k_{2i} C_{2i} e^{k_{2i}x+i\omega t},$$

$$u_3(x,\omega,t) = W_0 \sum_{i=1}^{6} g_{2i} C_{2i} e^{k_{2i}x+i\omega t}, \quad \gamma_c(x,\omega,t) = W_0 \sum_{i=1}^{6} C_{2i}(Hk_{2i} + g_{2i}) e^{k_{2i}x+i\omega t},$$

$$P(x,\omega,t) = W_0 E_3 A_3 \sum_{i=1}^{6} C_{2i} g_{2i} e^{k_{2i}x+i\omega t}. \tag{30a–e}$$

3. Results and discussions

3.1. Experiment

The experimental parameters are $h_1 = 0.8$ mm, $h_3 = 0.25$ mm, $h_2 = 4$ mm, $b_0 = 20$ mm, $L = 300$ mm, damping length = 100 mm, $E_1 = E_3 = 7.10 \times 10^{10}$ Pa, $\rho_1 = \rho_3 = 2.7 \times 10^3$ kg/m^3, $\rho_2 = 150$ kg/m^3, lg $G = 0.1015 \lg \omega/2\pi + 5.1817$, $\eta = 3.3 \times 10^{-6} \times (\omega/2\pi)^3 - 4.33 \times 10^{-4} \times (\omega/2\pi)^2 + 2.09 \times 10^{-2} \times (\omega/2\pi) + 0.1722$. The permanent magnets are made of NdFeB blocks ($20 \times 5 \times 5$ mm) with residual induction $B_r = 11,900$ G and demagnetized coercive force ${}_BH_c = 10,630$ Oe and intrinsic coercive force ${}_JH_c = 17,660$ Oe, and magnetized through x direction. The gap between two magnets is 1 mm. The base of the beam is subjected to the sinusoidally varying transverse displacement $0.2e^{i\omega t}$. The vibration of the beam at the tip is monitored. In Fig. 6, it can be seen that the first three resonance amplitudes are about 20% and 15% and 1%, respectively less than those without magnets, and the natural frequencies of MCLD are also less than those of PCLD. The theoretical values are in good agreement with experimental results.

3.2. Vibration attenuation mechanism

Analytical parameters chosen are the same as experimental ones. Fig. 7(a–e) show that the influence of dynamic magnetic force F_d on VEM strains γ_c and force P acting on the constraining layer. When a state of the first resonance exists, for the PCLD treatment, the maximal force P is 0.60 N (at $x \approx 45$ mm). At $x = 1$ mm, although the rotary angle is relatively very small, the amplitude of shear strains γ_c is about 8.2×10^{-3} rad, hence the longitudinal displacement becomes relatively high ($u_3 = 3.6 \times 10^{-2}$ mm), having a potential for producing strong dynamic magnetic force on the constraining layers. With attraction arrangement magnets, although the amplitude decreases, the maximal shear strain γ_c is still about 7.9×10^{-3} rad at $x = 1$ mm, resulting in dynamic magnetic force $P|_{x=L_1}$ of 0.35 N whereas the maximal force P_{max} is about 0.31 N at other locations. Hence, the effect of $P|_{x=L_1}$ on the sandwich beam is significant enough to reduce the

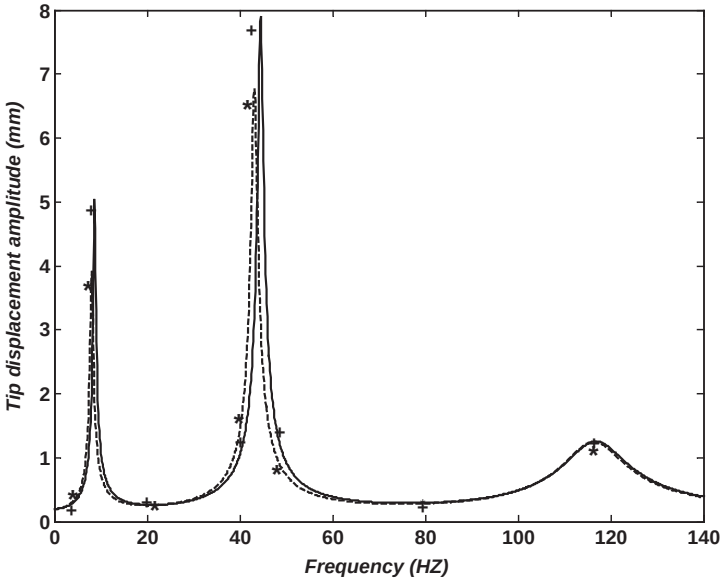

Fig. 6. Effect of MCLD on frequency response of beam (calculation: ---, MCLD; —, PCLD; experiment: ∗, MCLD; +, PCLD).

elastic potential energy of constraining layers and the primary layer and enhance the dissipation energy of the damping layers. The rise of the ratio of dissipation energy to the total system energy per cycle decreases the system resonance peaks. Similar conclusion can be obtained for the second mode.

3.3. Effect of the geometrical and physical parameters

The following conditions are made in the analysis: (1) $G_c = 2 \times 10^5(1 + 0.4\mathrm{i})$ (2) unless otherwise stated, the parameters are identical to those in the experiment.

3.3.1. Effect of physical parameters

(1) *Effect of VEM shear modulus*: Fig. 8(a) illustrates the variation of resonance peaks achieved by the PCLD/MCLD treatments with VEM shear modulus G. It can be seen for the PCLD treatment that a minimal resonance peak is only obtainable at a particular value of G_{opt} and that as G deviates from the G_{opt}, the resonance peak for the first mode would increase rapidly. The same phenomenon was also observed for the fully covered damped sandwich beam [10]. In practice, G would decrease resulting from the temperature rise in operation, and the VEM of optimal shear modulus G_{opt} is not always available. Therefore, a better damping is not easily obtained.

However, the improvement of MCLD for $G < G_{opt}$ is significant, whereas the improvement for $G > G_{opt}$ is not. The phenomenon can be explained as follows. For $G < G_{opt}$, the shear strain γ_c increases under the action of shear stress of the same value. As a result, the ratio of alternating magnetic force F_d to the maximal force P_{max} acting on the CL is increased, and the resonance peak is suppressed. For $G > G_{opt}$, higher the G, higher the P_{max} although the amplitude of shear

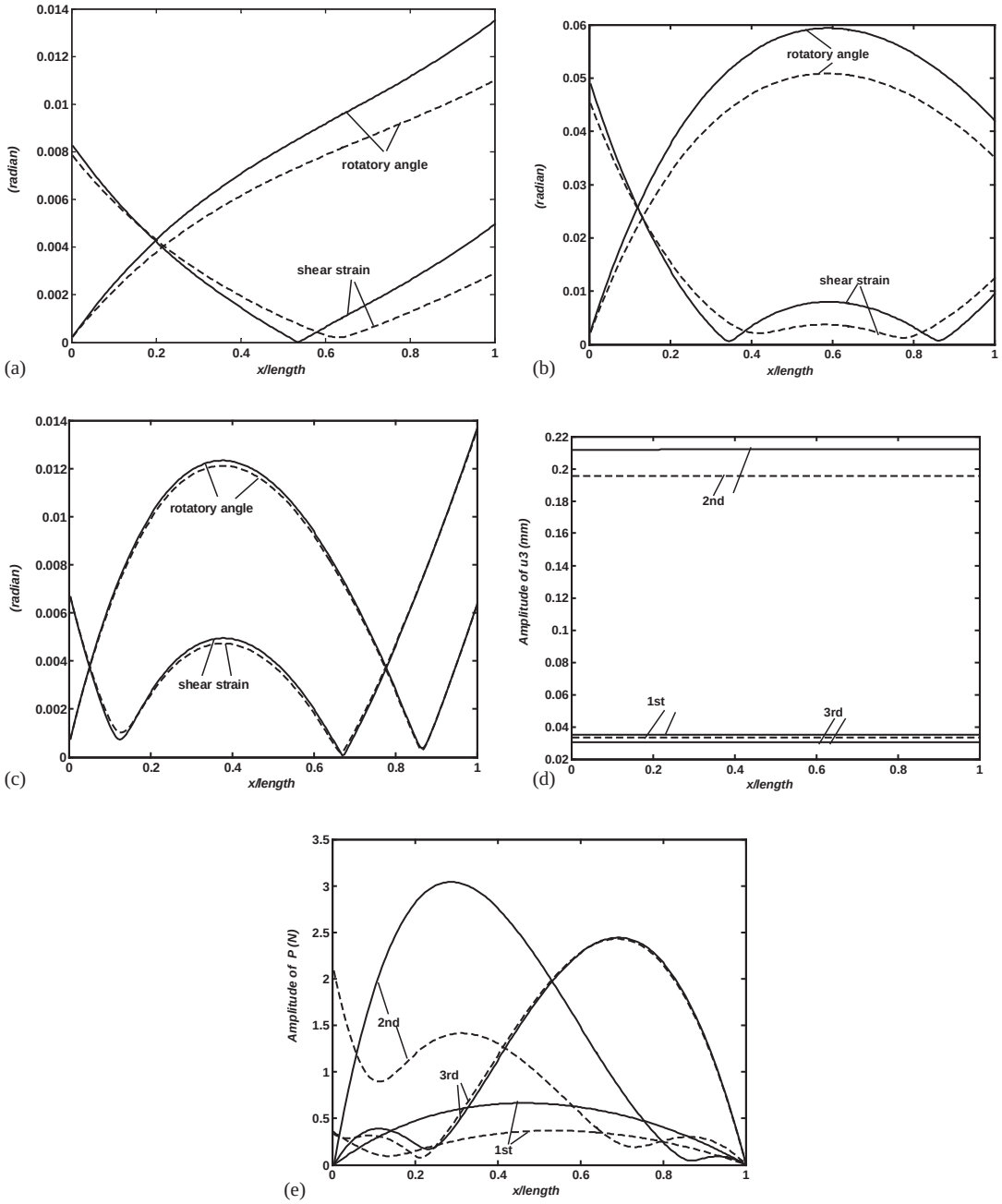

Fig. 7. Influence of MCLD/PCLD: (a) on amplitude of rotary angle θ and shear strain γ_c (1st mode), (b) on amplitude of rotary angle θ and shear strain γ_c (2nd mode); (c) on amplitude of rotary angle θ and shear strain γ_c (3rd mode), (d) on u_3, (e) on amplitude of force P on constraining layer (---, MCLD; —, PCLD).

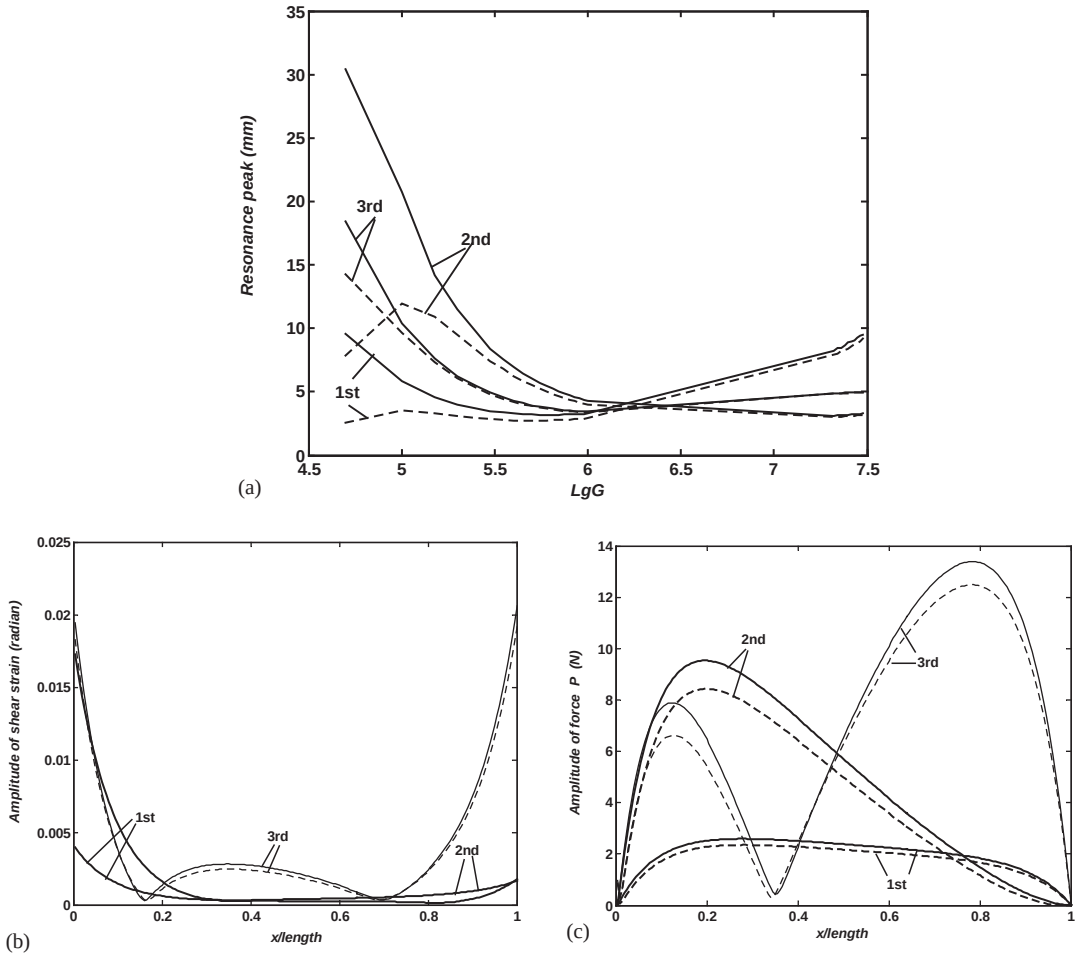

Fig. 8. Effect of VEM shear modulus G: (a) variation of resonance peaks with VEM shear modulus G, (b) influence of MCLD/PCLD on amplitude of shear strain γ_c, (c) influence of MCLD/PCLD on amplitude of force P on constraining layer, $G_c = 4 \times 10^6(1 + 0.4i)$ (- - -, MCLD; —, PCLD).

angle is not small. For example, for $G_c = 4 \times 10^6(1 + 0.4\text{i})$, although the amplitude of shear angle for the first mode at $x = 1$ mm is 4.2×10^{-3} rad, F_d is only 0.1 N, whereas $P_{max} = 2.2$ N acting on the CL (Fig. 8(b and c)). The ratio of F_d to P_{max} is small, not enough to affect the deformation of the sandwich beam. A similar conclusion can be obtained for the higher modes.

The analysis presented above shows that significant improvement of damping characteristics exists over a broad G range for $G < G_{opt}$. This implies that the limitation to the VEM for the MCLD is less than that for the PCLD, and the degeneration of damping characteristics because of temperature rise can be compensated for to some extent using the MCLD.

(2) *Effect of CL Young's modulus*: Fig. 9 illustrates the variation of resonance peaks with the CL Young's modulus E_3 with $E_1 = 2.1 \times 10^{11}$ Pa. These curves of MCLD are relatively parallel to those of PCLD, but there are large spaces between the two treatments. The spaces between curves also imply that the MCLD has significant improvement for different E_3's.

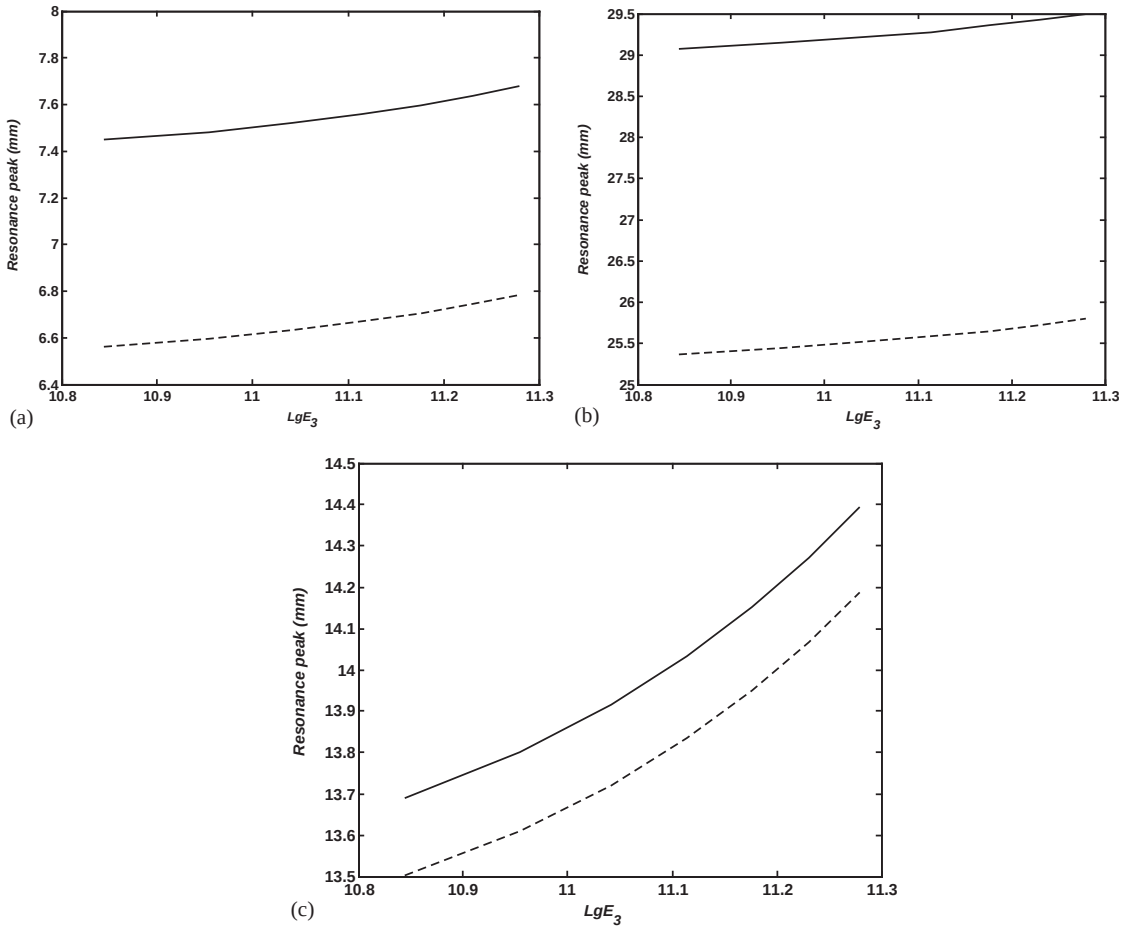

Fig. 9. Variation of resonance peaks with the CL Young's modulus E_3 with $E_1 = 2.1 \times 10^{11}$ Pa: (a) 1st mode, (b) 2nd mode, (c) 3rd mode (- - -, MCLD; —, PCLD).

3.3.2. *Effect of the geometrical parameters*

(1) *Effect of damping length*: Fig. 10(a) shows the vibration reduction ratios of the MCLD to the PCLD varying with the coverage length from length = 60 mm to full coverage for the first three modes. These curves reveal that treatment length affects the ratios in a non-uniform way. For the first mode, the MCLD treatment improves damping rather significantly over a large coverage length range; however, for the higher modes, the MCLD induces damping rather significantly in the beginning, but the curves descend rapidly while increasing the coverage, the improvement eventually becomes marginal. The reason is that for higher modes the amplitude of shear angles becomes relatively lower compared with that of shear angles at other locations as coverage length keeps increasing, causing weak dynamic magnetic force (see Fig. 10(b and c)). Hence, for a too long damping layer, using the MCLD induces less improvement of damping characteristics for higher modes. Suitable coverage length can simultaneously control vibration for the first several modes.

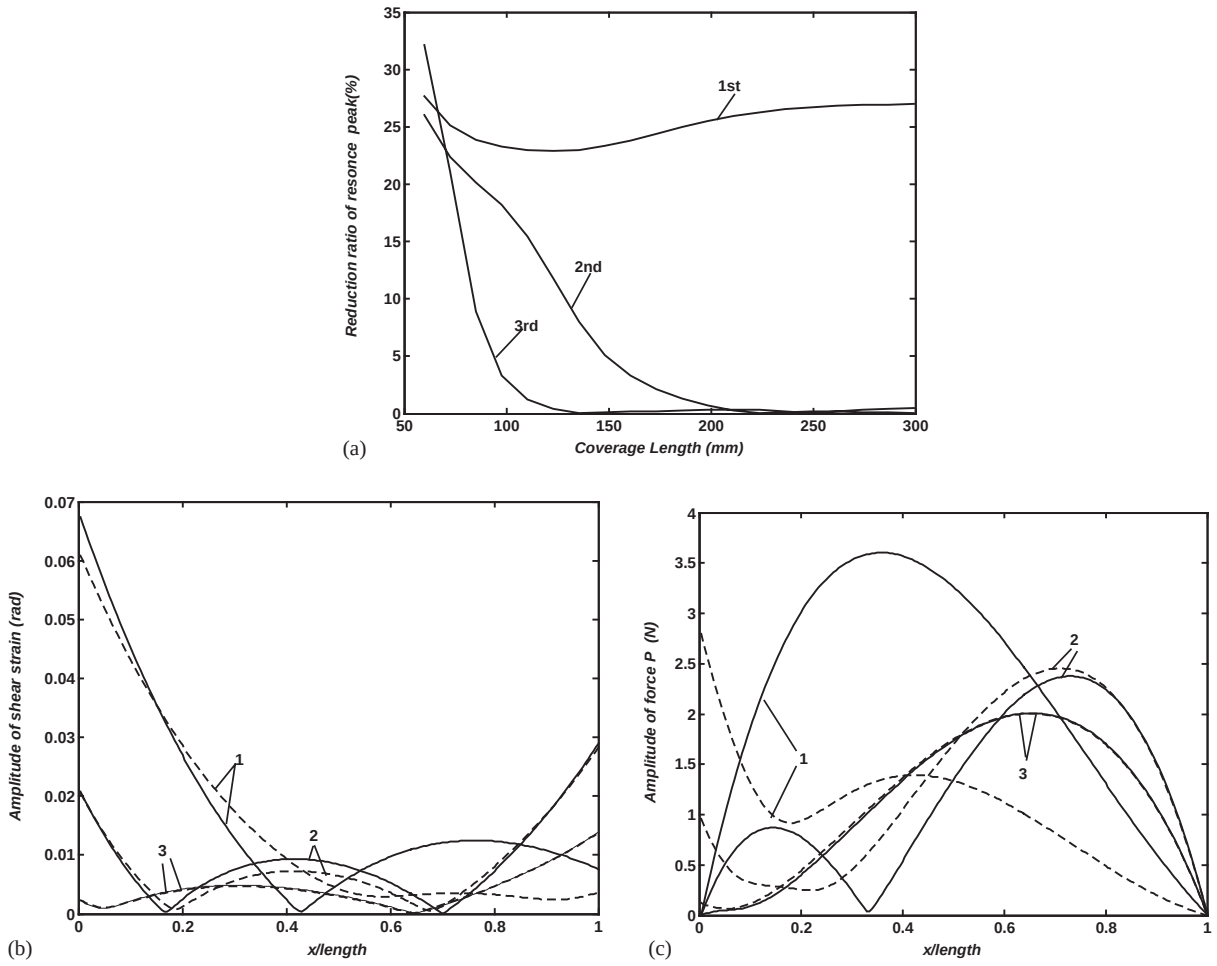

Fig. 10. Effect of coverage length: (a) variation of ratios of resonance peaks decrement with the coverage length, (b) influence of different damping length on amplitude of shear strain γ_c (2nd mode), (c) influence of different damping length on amplitude of force P on constraining layer (2nd mode) (---, MCLD; —, PCLD; 1, *length* = 80 mm; 2, *length* = 150 mm; 3, *length* = 200 mm).

(2) *Effect of VEM thickness*: As to the VEM thickness effects, Fig. 11 shows that for the PCLD, h_2's effects on resonance peaks are non-uniform. When h_2 is very thin, a small amount of h_2 increment improves damping drastically. Further increase of VEM thickness induces less significant damping. However, for the MCLD, as expected, because thicker VEM produces strong dynamical magnetic force F_d, the resonance peaks decrease rapidly as h_2 keeps increasing for the first two modes, the improvement is not significant because of the effect of damping length on the third mode. Therefore, the MCLD treatment has advantages over the PCLD for thicker VEM.

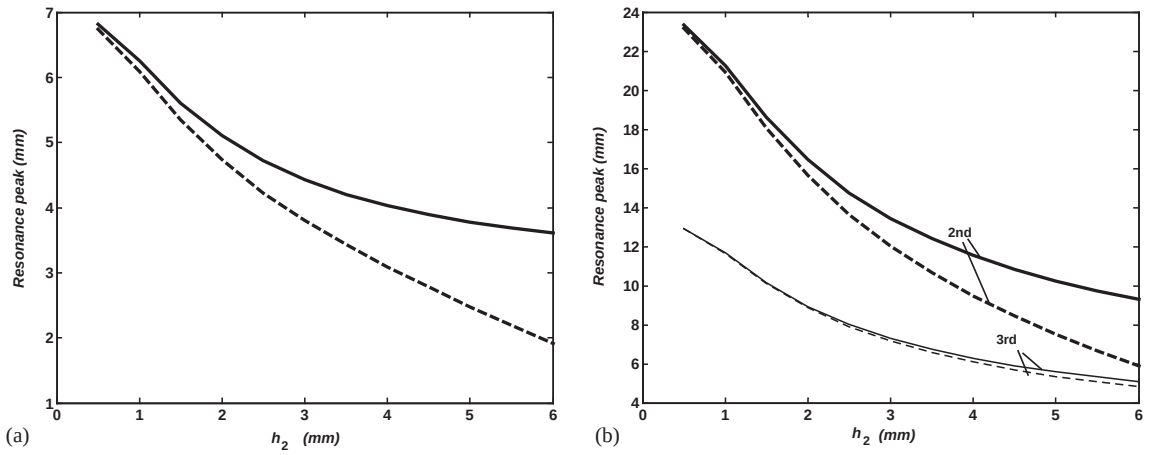

Fig. 11. Variation of resonance peaks with VEM thickness h_2: (a) 1st mode, (b) 2nd and 3rd modes (---, MCLD; —, PCLD).

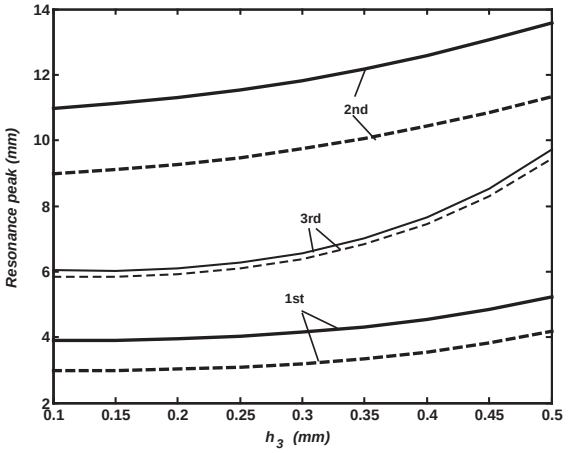

Fig. 12. Variation of resonance peaks with CL thickness h_3 (---, MCLD; —, PCLD).

(3) *Effect of CL thickness*: Fig. 12 illustrates the variation of resonance peaks with CL thickness h_3. It can be seen that the improvement of damping characteristics of the MCLD still exists.

3.4. Effect of magnetic stiffness

Fig. 13 illustrates the variation of resonance peaks with magnetic stiffness K_d. It can be seen that, if K_d is lower than some value K_0 ($K_0 \approx 1 \times 10^3$ N/m for 1st mode), using MCLD would have little improvement. Fortunately, the rare earth permanent magnets, such as NdFeB can supply enough high K_d as shown in Fig. 4. After K_d exceeds K_0, increasing K_d, drastically increases the resonance peaks. But for higher modes K_0 becomes higher. Hence enhancing dynamic magnetic force can significantly improve vibration reduction effect.

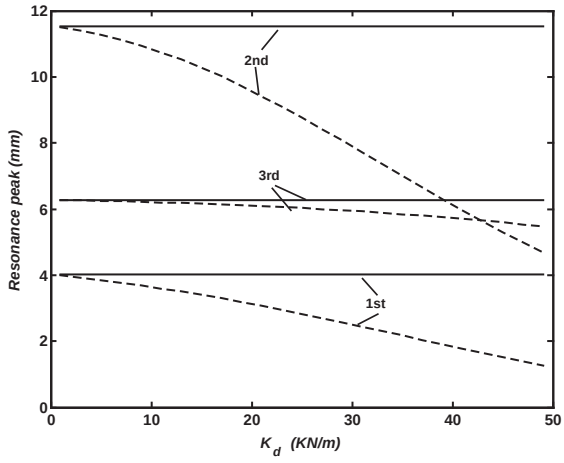

Fig. 13. Variation of resonance peaks with magnetic stiffness K_d (---, MCLD; —, PCLD).

4. Conclusions

In this paper, the differential equations of motion of a partially covered sandwich cantilever beam are derived employing Hamilton's principle. The modelling is validated experimentally. By analyzing the influence of permanent magnets on VEM's shear strains and force acting on the constraining layer, the vibration attenuation mechanism of the MCLD treatment versus the PCLD treatment is understood clearly. The effects of different physical and geometrical parameters on resonance peaks are evaluated. The following conclusions were obtained in order to determine the merits and limitations of MCLD treatments and to develop design guidelines:

(1) Significant improvement of the damping characteristics can be achieved by using the MCLD treatment. The analyses reveal that the variation amplitude of VEM shear angle at the root where permanent magnets are fitted is relatively high, producing relatively high dynamic magnetic force compared to the maximal force on the CL. The dynamic magnetic force is strong enough to reduce the elastic potential of the constraining layers and primary layer and enhance the dissipation energy of the damping layers. The rise of the ratio of dissipation energy to the total system energy per cycle decreases the resonance peaks.

(2) As the damping layer thickness increases to some extent, the use of the MCLD can significantly improve the damping characteristics of PCLD treatments.

(3) As the damping length increases, using MCLD is still effective in reducing vibration for the first mode, but the effect decreases drastically for higher modes as coverage length keeps increasing. Suitable damping length can simultaneously improve damping effects for the first several modes.

(4) The interaction between the magnets and the sandwich beam is sensitive to the VEM's shear modulus G. Increasing G decreases the improvment of the MCLD. The limitation to the VEM for the MCLD is less than that for the PCLD, and the degeneration of damping characteristics because of temperature rise can be compensated for to some extent using the MCLD.

(5) Using the MCLD has also effect on improving the damping characteristics for different Young's modulus and thickness of the CL.

(6) For lower magnetic stiffness K_d, using MCLD would have little improvement whereas resonance peaks would decrease drastically for higher magnetic stiffness as K_d keeps increasing.

Appendix A. Nomenclature

$\mathbf{B}$	magnetic induction
$\mathbf{H}$	magnetic field
$\mathbf{J}$, $\mathbf{J}'$	magnetization
$\mathbf{I}$, $\mathbf{I}'$	volume current density
$\mathbf{K}$, $\mathbf{K}'$	surface current density
$\mathbf{n}$, $\mathbf{n}'$	unit vector normal to the surfaces of the magnets
$D_{t1} = \frac{1}{12}E_1 b_0 h_1^3$	bending rigidity of the primary beam
E_i	Young's modulus of the ith layer
G	storage shear modulus
η	loss factor of the damping layer
$G_c = G(1 + \mathrm{i}\eta)$	complex shear modulus of damping layer
m_1	mass per unit length of the primary beam
$D_t = \frac{b_0(E_1 h_1^3 + 2E_3 h_3^3)}{12}$	bending rigidity of the sandwich section
m	mass density per unit length of sandwich section
m_{mag}	mass of a magnet
h_{mag}	thickness of a magnet
M_i	bending moment of cross-section
S_i	shear force of cross-section *length* length of coverage
L	total length of beam
h_i	thickness of the ith layer
ρ_i	mass density of the ith layer material
$A_i = bh_i$	transverse cross area of the ith layer
P	alternating axial force of the constraining layer
u_i	alternating axial displacement of ith layer
w_i	transverse displacement of the ith section
t	time
b_0	width of beam
$\mathrm{i} = \sqrt{-1}$	

References

[1] S. Kung, R. Singh, Vibration analysis of beams with multiple constrained layer damping patches, *Journal of Sound and Vibration* 212 (1998) 781–805.

[2] W. Shields, J. Ro, A. Baz, Control of sound radiation from a plate into an acoustic cavity using active piezoelectric damping composites, *Journal of Smart Materials and Structures* 7 (1998) 1–11.

[3] A. Baz, J. Ro, Actively controlled constrained layer damping, *Sound and Vibration Magazine* 28 (1994) 18–21.

[4] M. Ruzzene, J. Oh, A. Baz, Finite element modelling of magnetic constrained layer damping, *Journal of Sound and Vibration* 236 (2000) 657–682.
[5] A. Baz, S. Poh, Performance characteristics of the magnetic constrained layer damping, *Shock and Vibration* 72 (2000) 81–90.
[6] B. Tsui, The effect of intrinsic magnetic properties on permanent magnetic repulsion, *IEEE Transactions on Magnetics* 8 (2) (1972) 188–194.
[7] D. Ebihara, T. Suzuki, K. Imagawa, The reduction of lateral force by the arrangement of permanent magnets in the PM-type magnetic levitation device, *IEEE Transactions on Magnetics* 23 (5) (1987) 2347–2349.
[8] D. Ebihara, K. Imagawa, Analysis of levitating and lateral forces of magnetc levitating system of permanent magnet repulsion type, *Electrical Engineering in Japan* 106 (6) (1986) 135–142.
[9] D. Mead, S. Markus, The forced vibration of a three-layer damped sandwich beam with arbitrary boundary condition, *Journal of Sound and Vibration* 10 (1969) 163–175.
[10] D. Ahid, Nashif, I. David, *Vibration Damping*, Wiley, New York, 1985.